

Low-Noise Near-Infrared Photomultiplication Organic Photodetectors Enabled by Donor-Sidechain Steric Engineering

Downloaded from: https://research.chalmers.se, 2026-11-24 15:47 UTC

Citation for the original published paper (version of record):

Gao, J., Wu, J., Wang, Z. et al (2026). Low-Noise Near-Infrared Photomultiplication Organic Photodetectors Enabled by Donor-Sidechain
Steric Engineering. ACS Applied Electronic Materials, 8(21): 9638-9646.
http://dx.doi.org/10.1021/acsaelm.6c01773

N.B. When citing this work, cite the original published paper.

research.chalmers.se offers the possibility of retrieving research publications produced at Chalmers University of Technology. It covers all kind of research output: articles, dissertations, conference papers, reports etc. since 2004. research.chalmers.se is administrated and maintained by Chalmers Library

(article starts on next page)

ACS APPLIED ELECTRONIC MATERIALS

Open Access

This article is licensed under CC-BY 4.0

pubs.acs.org/acsaelm

Article

Low-Noise Near-Infrared Photomultiplication Organic Photodetectors Enabled by Donor-Sidechain Steric Engineering

Published as part of ACS Applied Electronic Materials special issue "Photo-Detecting and Light-Emitting Materials and Devices in the Near Infrared and Shortwave Infrared Spectral Ranges".

Jing Gao, Jingnan Wu, Zhuangmiao Wang, Yu Tang, Donghong Yu,* Ergang Wang,* and Furong Zhu*

Cite This: *ACS Appl. Electron. Mater.* 2026, 8, 9638−9646

Read Online

ACCESS | Metrics & More | Article Recommendations | Supporting Information

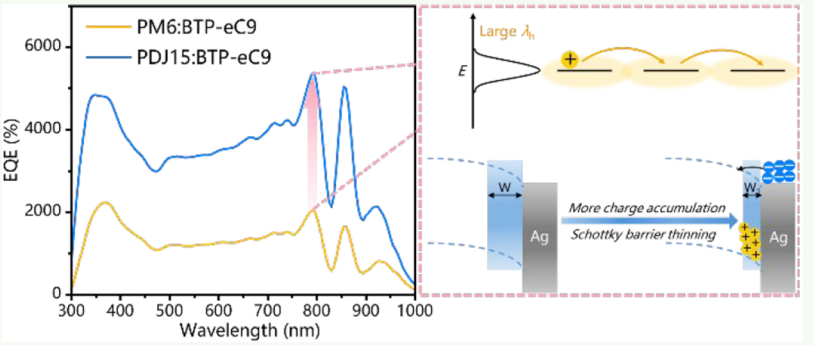

ABSTRACT: Achieving low dark current remains a major challenge for photomultiplication-type organic photodetectors (PM-OPDs). In this work, we show that steric engineering of donor side chains, through incorporation of bulky fluorinated alkoxyphenyl sidechains into a BDT-based polymer donor, is an effective approach to reduce dark current while enhancing photomultiplication. The polymer PDJ15 exhibits a more twisted backbone, reduced donor−acceptor packing and a higher hole reorganization energy (0.24 eV) relative to PM6, collectively impeding hole transport and assisting in trap-assisted charge injection. A specific detectivity of 4.6×10^{12} Jones at 800 nm was achieved for a PDJ15:BTP-eC9 PM-OPD under 1.0 V, outperforming the PM6:BTP-eC9-based control device (2.7×10^{11} Jones) operated under the same condition. The results reveal that donor-sidechain engineering is an effective molecular design strategy for high-gain and low-noise near-infrared PM-OPDs.

KEYWORDS: *near-infrared, organic photodetectors, photomultiplication, donor-sidechain engineering, dark current mitigation*

1. INTRODUCTION

Organic semiconducting materials with extended π-conjugated backbones are fundamental to advanced optoelectronic devices, making it crucial to elucidate how chemical structures dictate their charge-transport properties for the design of high-performance systems.[1−5] In these π-conjugated frameworks, charge transport operates via coherent mechanisms over short distances and transitions to hopping transport across longer ranges.[6−9] Despite considerable progress in optimizing intermolecular charge transport, the influence of donor molecular structure on localized-state hopping, charge trapping, and dark current mitigation in photomultiplication-type organic photodetectors (PM-OPDs) remains poorly understood.[10−13]

The performance of the PM-OPDs is closely associated with the trap-assisted charge injection under illumination. In hole-trap-based PM-OPDs, the accumulation of the trapped photogenerated holes in the bulk heterojunction (BHJ) or at BHJ/electrode interfaces induces pronounced band bending, which facilitates electron injection via tunnelling. Therefore, understanding the interplay between donor molecular structure and hole transport properties, as well as the impact of donor-sidechain engineering on dark current mitigation, is crucial for achieving achieving high-performance PM-OPDs.[14−16] The rational design of donor polymers with balanced charge trapping, optimized carrier mobility, and suitable energy level alignment with nonfullerene acceptors for achieving high-performance near-infrared (NIR) PM-OPDs has become

Received: August 17, 2026
Revised: October 11, 2026
Accepted: October 11, 2026
Published: October 19, 2026

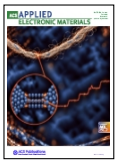

Downloaded from pubs.acs.org/aaembp/article-pdf/8/21/9638/6890798/el-2026-01773w.pdf by CHALMERS UNIV OF TECHNOLOGY user on 23 November 2026

© 2026 The Author(s). Published by American Chemical Society

https://doi.org/10.1021/acsaelm.6c01773
ACS Appl. Electron. Mater. 2026, 8, 9638−9646

increasingly important and has attracted considerable attention.[17−19] Recent advances in NIR OPDs through optical modulation and interface engineering have enabled visible-blind, high-contrast NIR imaging and enhanced device integration for real-time sensor arrays.[20] The bias-switchable dual-mode OPDs also allow self-aligned imaging across both NIR-I and NIR-II regions.[21] These developments reveal the rapid progress and research effort on development of high-performance, and application-driven NIR photodetector technologies.

Advancements in NIR PM-OPDs have largely focused on blend-ratio manipulation, acceptor molecular engineering, interfacial optimization, and innovative device architectures. Trap-assisted photomultiplication in low-acceptor concentration P3HT:$PC_{71}BM$ PM-OPDs was reported,[22,23] where isolated fullerene domains functioned as electron traps to establish interfacial band bending and facilitate tunnelling injection. This strategy was later extended to non-fullerene acceptors, enabling wider spectral response and improved device stability.[24,25]

Various interfacial engineering strategies, e.g., the incorporation of hole-blocking layers, MoO_3-assisted traps, and interfacial modification, have been adopted to modulate charge accumulation and mitigate leakage currents in PM-OPDs.[26,27] It shows that the distribution of photogenerated carriers and the profile of optical field play critical roles in enhancing the performance of PM-OPDs. Building on these insights, advanced device architectures, including dual-BHJ OPDs,[28,29] inverted NIR OPDs[30] and short-wave infrared (SWIR) photodetectors,[31,32] have been developed. Recently, a charge trap gradient BHJ strategy has been demonstrated as an effective approach for mitigating dark current in PM-OPDs, enabling simultaneously reduced leakage current and enhanced tunneling charge injection for improved sensitivity at low operating voltage.[33] Collectively, these studies reveal the impacts of film morphology, interfacial properties, optical field distribution, and trap engineering on the device performance. However, the effect of intrinsic donor molecular structure, particularly donor-sidechain steric hindrance and hole reorganization energy (λ_h) on dark current mitigation in PM-OPDs, remains relatively unexplored and warrants further investigation.

In this work, a donor-sidechain steric engineering strategy was employed to mitigate dark current in PM-OPDs by incorporating bulky fluorinated alkoxyl phenyl sidechains onto a BDT-based donor backbone. BTP-eC9 served as the acceptor to enable a direct comparison between the conventional PM6 donor and the newly developed PDJ15, thereby revealing the impact of increased steric hindrance on device characteristics. The PDJ15:BTP-eC9 bulk heterojunction, fabricated at a 7:100 weight ratio, demonstrated enhanced steric bulk and higher λ_h compared to PM6:BTP-eC9. These modifications effectively suppressed dark current, resulting in a marked improvement in the performance of NIR PM-OPDs.

2. RESULTS AND DISCUSSION

In this context, a new donor polymer, PDJ15, was developed by incorporating mono-fluorinated alkoxyl phenyl as bulky sidechains into a BDT-based backbone. This sidechain engineering strategy endows PDJ15 with larger steric hindrance than the benchmark donor PM6 (containing 2-ethylhexyl-substituted thiophene units shown in Figure 1a) with its synergistic electron induction and conjugation characteristics. Such structural modulation is expected to affect molecular packing and intermolecular electronic coupling, thereby influencing charge-transport behavior. The synthetic route and structural characterization are illustrated in Scheme S1 and Figures S1 and S2. Compared with PM6, PDJ15 introduces larger steric hindrance and fluorine-induced electronic modulation, which are expected to influence backbone packing, intermolecular electronic coupling and charge transport. GPC analysis gave M_n = 24.2 kDa, M_w = 70.3 kDa and PDI = 2.90 (Figure S3 and Table S1). The optical properties of the donor polymers were analyzed using UV−vis absorption spectroscopy. As depicted in Figure 1b, both neat PM6 and PDJ15 films exhibit broad absorption bands, consistent with their highly conjugated backbones. Compared with PM6, PDJ15 shows a slightly red-shifted absorption onset. After blending with BTP-eC9, both blend films maintain complementary spectral coverage extending into the near-infrared region, which is favorable for broadband photoresponse in PM-OPDs.

To further understand the influence of sidechain fluorination on the electronic structure, cyclic voltammetry was performed to determine the frontier molecular orbital energy levels of the donor polymers (Figure 1c,d). PDJ15 has a higher LUMO energy level of −3.13 eV compared to that of PM6 (−3.50 eV), indicating that the introduction of bulky fluorinated alkoxyphenyl sidechains effectively modulates the electronic structure of the donor polymer. This upward shift in the LUMO level is beneficial for suppressing reverse-bias electron injection while maintaining efficient photoinduced charge generation in the PM-OPDs. The corresponding frontier energy levels, together with the optical bandgaps (E_g^{opt}) estimated from the UV−vis−NIR absorption onsets, are summarized in Table S2, providing a comprehensive picture of the donor−acceptor energetic alignment in the PM6:BTP-eC9 and PDJ15:BTP-eC9 systems.

The intermolecular packing geometries of the donor:BTP-eC9 complexes were analyzed using density functional theory (DFT) at the B3LYP/6-31G(d) level with Grimme's D3(BJ) dispersion correction. Frequency calculations were performed at the same level of theory to confirm the optimized geometries. As illustrated in Figure 2, PM6 exhibits a dihedral angle of 51.57° along the conjugated backbone, whereas PDJ15 shows two torsional angles of 23.96 and 60.86 ° due to the incorporation of bulky mono-fluorinated alkoxylphenyl sidechains. These larger torsional distortions indicate stronger steric hindrance and reduced backbone planarity in PDJ15. The optimized donor−acceptor interfacial structures reveal that PM6 forms a more compact packing with BTP-eC9, with a π−π stacking distance of 3.50 Å and an interaction energy of −81.19 kcal·mol^{-1}. In contrast, PDJ15 shows a slightly increased intermolecular distance of 3.66 Å and a weaker interaction energy of −76.61 kcal·mol^{-1}, indicating a looser donor−acceptor interfacial packing. These results suggest that the bulky fluorinated phenyl sidechains in PDJ15 not only increase backbone distortion but also weaken intermolecular electronic coupling at the donor−acceptor interface. The resulting loose molecular packing is unfavorable for electron transport, thereby contributing to the reduced dark current observed in PDJ15:BTP-eC9-based devices.

The hole reorganization energies (λ_h) of PM6 and PDJ15 were calculated using the four-point method based on Marcus electron-transfer theory. The detailed computational methodology is provided in the Supporting Information (Figure S4 and

Downloaded from pubs.acs.org/aaembp/article-pdf/8/21/9638/6907982/el-2026-01773w.pdf by CHALMERS UNIV OF TECHNOLOGY user on 23 November 2026

https://doi.org/10.1021/acsaelm.6c01773
ACS Appl. Electron. Mater. 2026, 8, 9638−9646

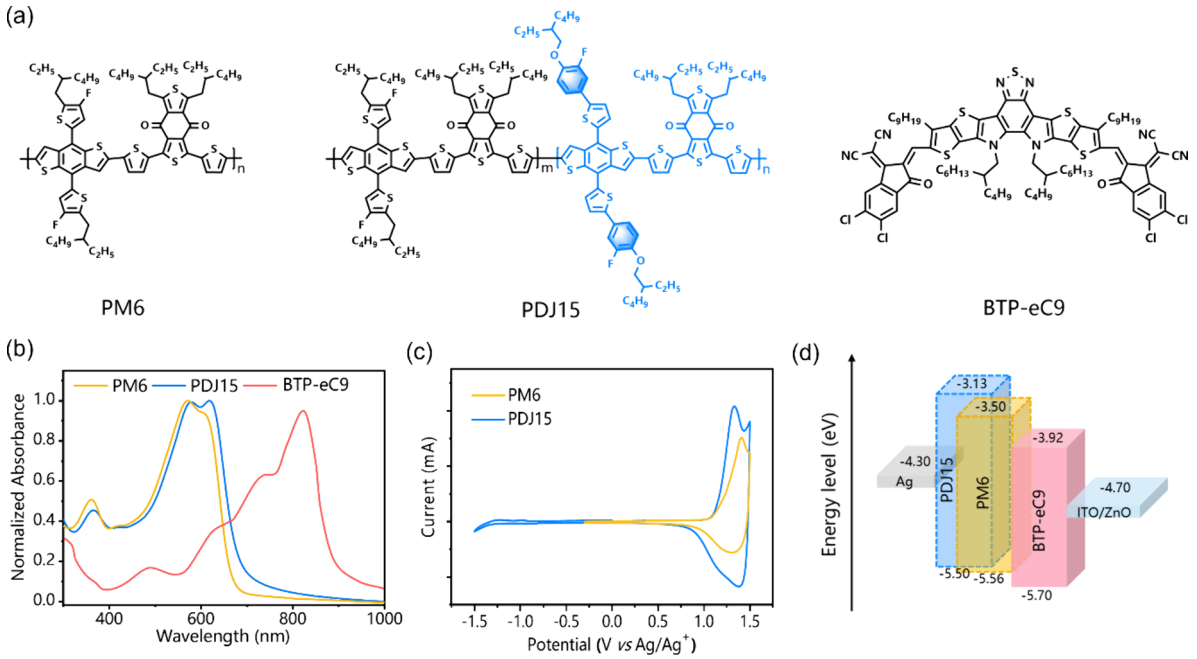

Figure 1. (a) Molecular structures of active-layer materials PM6, PDJ15, and BTP-eC9, (b) normalized absorption spectra of the neat PM6, PDJ15, and BTP-eC9 films, (c) cyclic voltammetry characteristics of PM6 and PDJ15, and (d) schematic illustration of the energy level alignment of the functional materials used in the PM-OPDs.

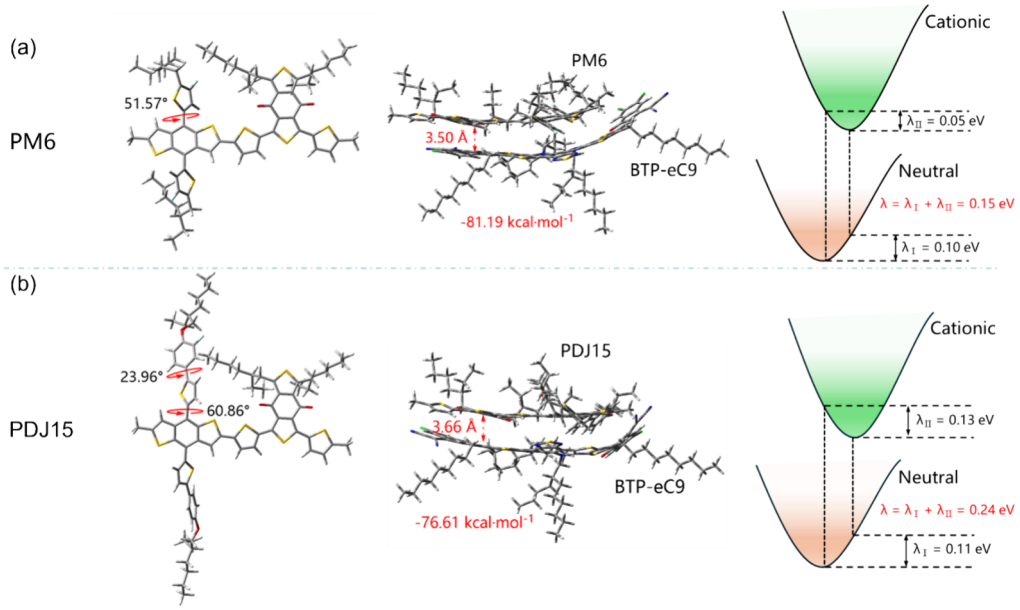

Figure 2. Theoretical analysis of (a) PM6 and (b) PDJ15, showing dihedral angles between the conjugated backbone and the substituted phenyl side chains, optimized intermolecular packing diagrams with BTP-eC9, and visualized λ_h from DFT-optimized cationic and neutral geometries.

eq S1). PDJ15 has a larger λ_h of 0.24 eV as compared to that of PM6 (0.15 eV). The increase in λ_h originates from the bulky mono-fluorinated phenyl sidechain in PDJ15, which introduces stronger steric congestion and greater conformational distortion into the polymer backbone. Compared with PM6, the reduced backbone planarity and disrupted π-conjugation continuity in PDJ15 result in more pronounced geometric relaxation between the neutral and cationic states during oxidation, thereby increasing the energetic cost associated with hole transfer. Within the Marcus hopping picture, the hole-transfer rate (k_h) can be expressed as:

$$k_h \propto \exp\left[-\frac{(\Delta G - \lambda_h)^2}{4k_B T\,\lambda_h}\right] \quad (1)$$

where ΔG is the change in free energy for charge transfer, k_B denotes the Boltzmann constant, and T represents the absolute

https://doi.org/10.1021/acsaelm.6c01773
ACS Appl. Electron. Mater. 2026, 8, 9638−9646

Downloaded from pubs.acs.org/aaembp/article-pdf/8/21/9638/6907982/el-2026-01773w.pdf by CHALMERS UNIV OF TECHNOLOGY user on 23 November 2026

temperature. For intradomain hole hopping in a relatively homogeneous donor phase, ΔG is usually small. Under this condition, an increase in λ_h leads to a lower hopping rate and thereby a lower hole mobility. Unlike molecular systems designed to achieve efficient intramolecular hopping transport by minimizing energy reorganization, the influence of PDJ15 with a relatively large λ_h on the performance of PM-OPDs is not yet fully understood.

To unravel how donor molecular structure affects photodetector behavior, we systematically investigated the charge-transport characteristics of the donor polymers and their corresponding blend devices. Hole-only devices based on neat donor polymer films were first fabricated and analyzed using the space-charge-limited current (SCLC) method. As shown in Figure S5a, the PDJ15:BTP-eC9-based hole-only device exhibits a lower hole mobility (μ_h) than its PM6:BTP-eC9-based counterpart, with a value of 1.6×10^{-4} cm^2 V^{-1} s^{-1} compared with 3.9×10^{-4} cm^2 V^{-1} s^{-1} for PM6.

To clarify the role of electron transport in dark-current suppression, electron-only devices made with PM6:BTP-eC9 and PDJ15:BTP-eC9 blend films, prepared using the blend systems with a weight a ratio of polymer to donor of 7:100 were characterized by the SCLC method (Figure S5b). According to the Mott–Gurney law, the electron mobility (μ_e) was extracted from the current density–voltage (J–V) characteristics in the SCLC regime. PM6:BTP-eC9 exhibits a μ_e of 4.7×10^{-4} cm^2 V^{-1} s^{-1}, while PDJ15:BTP-eC9 shows a much lower value of 2.4×10^{-4} cm^2 V^{-1} s^{-1}. This result indicates that the bulky fluorinated alkoxylphenyl sidechains in PDJ15 hinder electron transport, which helps suppress undesired dark current. As schematically illustrated in Figure 3a, the hindered hole transport in PDJ15 retards hole extraction and prolongs the residence time of photogenerated holes in the donor-rich regions and near the photoactive-layer/Ag interface. The accumulated holes enhance the local electric field and interfacial band bending, thereby narrowing the effective Schottky barrier and facilitating electron tunneling injection from the Ag electrode into the active layer.

Photocurrent density-effective voltage (J_{ph}–V_{eff}) characteristics of the PM-OPDs were analyzed. $J_{ph} = J_L - J_D$, where J_L and J_D are the current densities measured for the PM-OPDs under illumination and in the dark. $V_{eff} = V_0 - V_a$, where V_0 is the built-in potential in the device and V_a is the applied bias. The behavior of charge accumulation in PM-OPDs, e.g., the hole traps induced by the polymers PDJ15 and PM6 in the BHJ, can be analyzed using the slope of the J_{ph}–V_{eff} characteristics, as expressed by the following equation devices:[33]

$$\text{Slope} = \frac{d(\log J_{ph})}{d(\log V_{eff})} \quad (2)$$

Figure 3b presents the slopes and log–log plots of J_{ph}–V_{eff} measured for devices based on PM6:BTP-eC9 and PDJ15:BTP-eC9. The results show that the PDJ15:BTP-eC9 PM-OPD generates a higher photocurrent compared to the PM6:BTP-eC9 control device. Both PM-OPDs exhibit an observable hump in the slope within the V_{eff} range measured in the work, indicating that photogenerated holes accumulate in the active layers under these conditions. It shows that the accumulation of trapped holes at the PDJ15:BTP-eC9/Ag interface is apparently greater than at the PM6:BTP-eC9/Ag

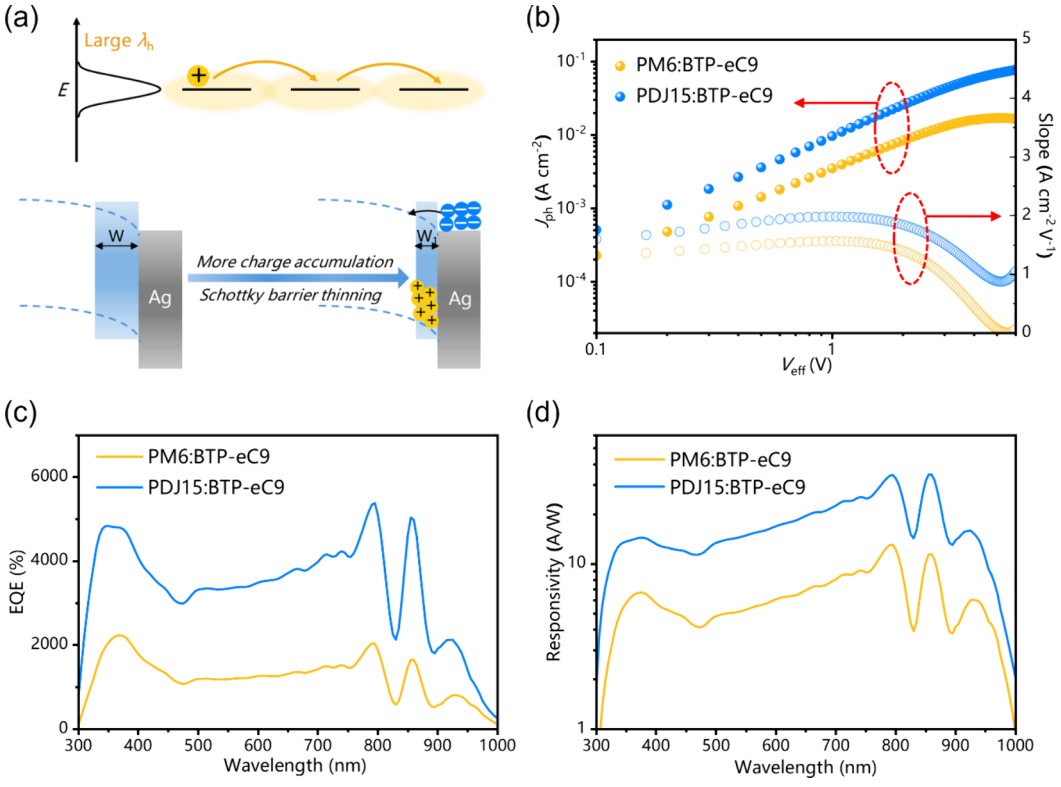

Figure 3. (a) Schematic illustration of depicting hopping transport and Schottky barrier thinning modulation via controlled hole trapping in PM-OPDs, (b) J_{ph}–V_{eff} characteristics and corresponding slopes, (c) EQE spectra at 1.0 V, and (d) $R(\lambda)$ spectra at 1.0 V.

https://doi.org/10.1021/acsaelm.6c01773
ACS Appl. Electron. Mater. 2026, 8, 9638–9646

Downloaded from pubs.acs.org/aaembp/article-pdf/8/21/9638/6907982/el-2026-01773w.pdf by CHALMERS UNIV OF TECHNOLOGY user on 23 November 2026

interface in the control device. This higher density of trapped holes enhances band bending, which in turn assists in enhanced tunneling electron injection in the PDJ15:BTP-eC9 PM-OPD. These findings are consistent with the external quantum efficiency, EQE(λ), and spectral responsivity, $R(\lambda)$, results shown in Figure 3c,d, further confirming the improved performance of the PDJ15:BTP-eC9 PM-OPD.

The restrained hole transport in PDJ15 is also closely related to its enhanced photomultiplication behavior. As illustrated in Figure 3c, the PDJ15:BTP-eC9 PM-OPD exhibits a markedly higher EQE than the PM6:BTP-eC9-based device, especially in the near-infrared region. Under a forward bias of 1.0 V, the EQE of the PDJ15:BTP-eC9-based device reaches 5380% at 800 nm, substantially higher than that of the PM6:BTP-eC9-based device (2040% at 800 nm) under the same conditions. The responsivity $R(\lambda)$ calculated from EQE spectra, The following formula can be utilized to obtain the $R(\lambda)$ spectra of PM-OPDs:

$$R(\lambda) = \mathrm{EQE}(\lambda)\ \frac{q}{h\nu} \tag{3}$$

A $R(\lambda)$ of 34.5 A W^{-1} at 800 nm was obtained for the PDJ15:BTP-eC9 PM-OPD operated at 1.0 V, which is evidently higher than that of PM6 (13.1 A W^{-1}) operated under the same condition, as shown in Figure 3d. This enhancement can be attributed to the larger λ_h of PDJ15, which increases the activation barrier for hole hopping and slows hole extraction. As a result, photogenerated holes can remain trapped for a longer time near photoactive layer/Ag interface, thereby promoting stronger interfacial band bending and more efficient electron tunneling injection. The stability of the PDJ15:BTP-eC9 PM-OPD under duty-cycled illumination was evaluated by monitoring its temporal photoresponse at 1.0 V over 6000 s using a modulated 600 nm LED light source, as shown in Figure S6. The device exhibited well-defined and repeatable on-off photocurrent transitions throughout the test period, indicating robust operational stability and reliable response under prolonged, cycle-repeated illumination.

To further examine the influence of charge transport on device operation, the current density−voltage (J−V) characteristics of the PM6:BTP-eC9- and PDJ15:BTP-eC9 PM-OPDs in the dark were recorded (Figure 4a). The PDJ15:BTP-eC9-based device consistently shows a much lower dark current density than the PM6:BTP-eC9-based counterpart across the measured bias range. At 1 V, the dark current density decreases from 1.8×10^{-5} A cm^{-2} for PM6 to 1.4×10^{-6} A cm^{-2} for PDJ15. The evident reduction in dark current is associated with the charge transport in the PDJ15:BTP-eC9 active layer. The enlarged λ_h and reduced carrier mobility in PDJ15 are responsible for the mitigation of the leakage current.

The noise spectral density (S_n) of the PM-OPDs was measured at 1.0 V (see Figure 4b). Results show that the PDJ15:BTP-eC9 PM-OPD has significantly lower noise compared to the PM6:BTP-eC9-based device. At 100 Hz, for example, the PDJ15:BTP-eC9 PM-OPD exhibits an S_n value of 1.5×10^{-12} A $Hz^{-1/2}$, which is substantially lower than the 7.1×10^{-12} A $Hz^{-1/2}$ observed for the PM6:BTP-eC9 control device.

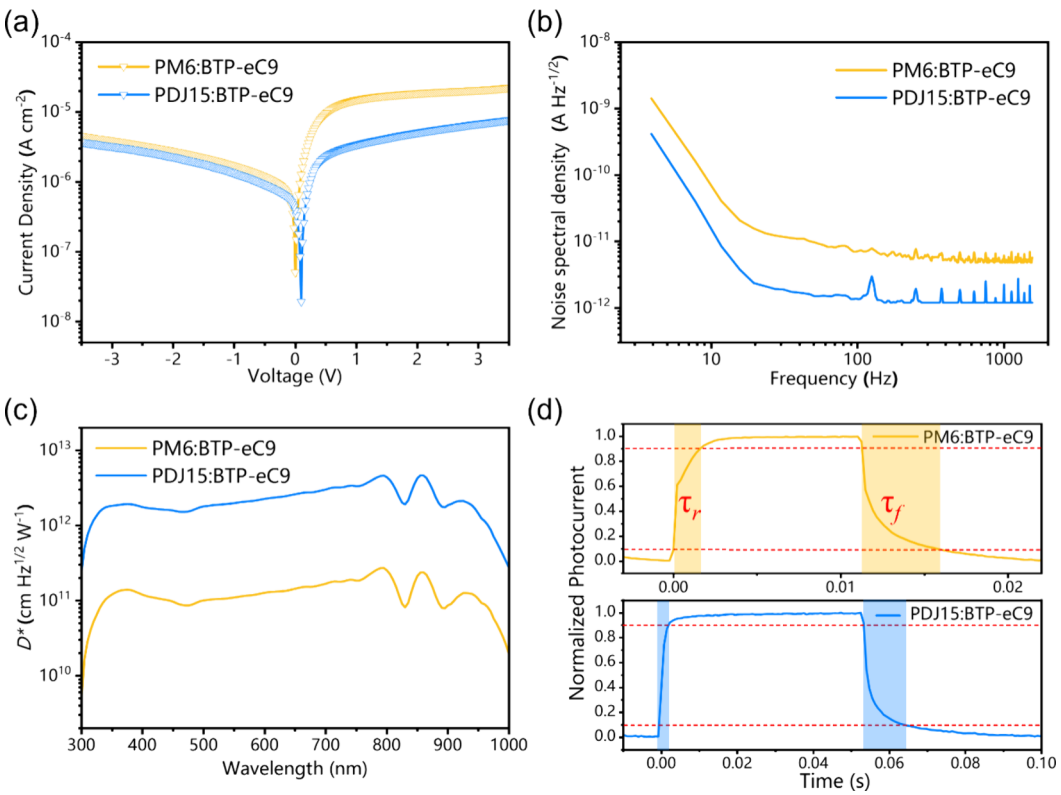

Figure 4. (a) Dark J−V characteristics, (b) S_n at 1.0 V, (c) $D^*(\lambda)$ at 1.0 V, and (d) photoresponse times under 680 nm light illumination with an intensity of 3.2 mW cm^{-2} for the PDJ15:BTP-eC9 and M6:BTP-eC9 PM-OPDs.

https://doi.org/10.1021/acsaelm.6c01773
ACS Appl. Electron. Mater. 2026, 8, 9638−9646

Downloaded from pubs.acs.org/aaembp/article-pdf/8/21/9638/6907982/el-2026-01773w.pdf by CHALMERS UNIV OF TECHNOLOGY user on 23 November 2026

This reduced noise is closely correlated with the lower dark current shown by the PDJ15:BTP-eC9 PM-OPD, as illustrated in Figure 4a.

Specific detectivity (D^*) is also an essential parameter that describes detection capability of the photodetector, which can be computed by referring to the formula as follows:

$$D^*(\lambda) = \frac{\sqrt{A} \times R(\lambda)}{S_n} \quad (4)$$

where A is the effective device area, $R(\lambda)$ is the responsivity, and S_n is the noise current spectral density measured under a bias of 1.0 V. The D^* spectra of the PM-OPDs operated at 1.0 V are shown in Figure 4c. At 100 Hz, the PDJ15:BTP-eC9 PM-OPD exhibits a D^* value of 4.6×10^{12} Jones at 800 nm, which is substantially higher than the 2.7×10^{11} Jones measured for the PM6:BTP-eC9 device. This significant improvement results from the high EQE and low dark current of the PDJ15:BTP-eC9 PM-OPD. The effectiveness of side-chain engineering in PDJ15 on the performance enhancement of the PM-OPD is clearly manifested.

The photoresponse times of the PM-OPDs were evaluated under illumination with a 680 nm LED light source. At an applied bias of 1.0 V, the PDJ15:BTP-eC9 PM-OPD demonstrated a rise time (τ_r) of 1.6 ms and a fall time (τ_f) of 4.6 ms, as shown in Figure 4d. In comparison, the PM6:BTP-eC9 PM-OPD exhibited a longer τ_r of 1.9 ms and a significantly longer τ_f of 10.2 ms. The considerably shorter photoresponse times achieved by the PDJ15:BTP-eC9 PM-OPD reflect a much higher photoresponse speed than that of the PM6:BTP-eC9-based control device, enabling the device to respond more rapidly and efficiently to changes in light intensity. This enhanced temporal performance suggests that the PDJ15:BTP-eC9 PM-OPD is particularly well-suited for applications that demand rapid and sensitive light detection. The improved photoresponse dynamics can be attributed to the optimized material properties and device architecture enabled by side-chain engineering in PDJ15, further broadening the potential utility of these high-performance PM-OPDs.

The influence of donor-sidechain steric modulation and λ_h was further examined using a newly developed polymer, PDJ16, which is a fluorinated analogue structurally related to PDJ15, as shown in Figure 5. The impact of donor-sidechain steric engineering on the performance of PDJ16:BTP-eC9 PM-OPDs was evaluated. PDJ16, having a sterically twisted backbone, exhibited dihedral angles of 17.01 and 57.42°. Computational analysis indicated that an intermolecular separation of 3.64 Å and a binding energy of −78.53 kcal mol^{-1} were present in the PDJ16:BTP-eC9 blend, suggesting favorable donor−acceptor interactions despite the non-planar geometry of the donor. Further investigation into the neutral and cationic forms of PDJ16 yielded a λ_h of 0.17 eV, supporting its role as a trend-consistent analogue for assessing the steric engineering strategy. It shows that even with a twisted backbone, PDJ16 maintained strong donor−acceptor association and effective charge transport, revealing the potential of sidechain engineering for further performance optimization in PM-OPDs.

The hole and electron mobilities in the PDJ16:BTP-eC9 blend layer, used for PM-OPD, were analyzed using

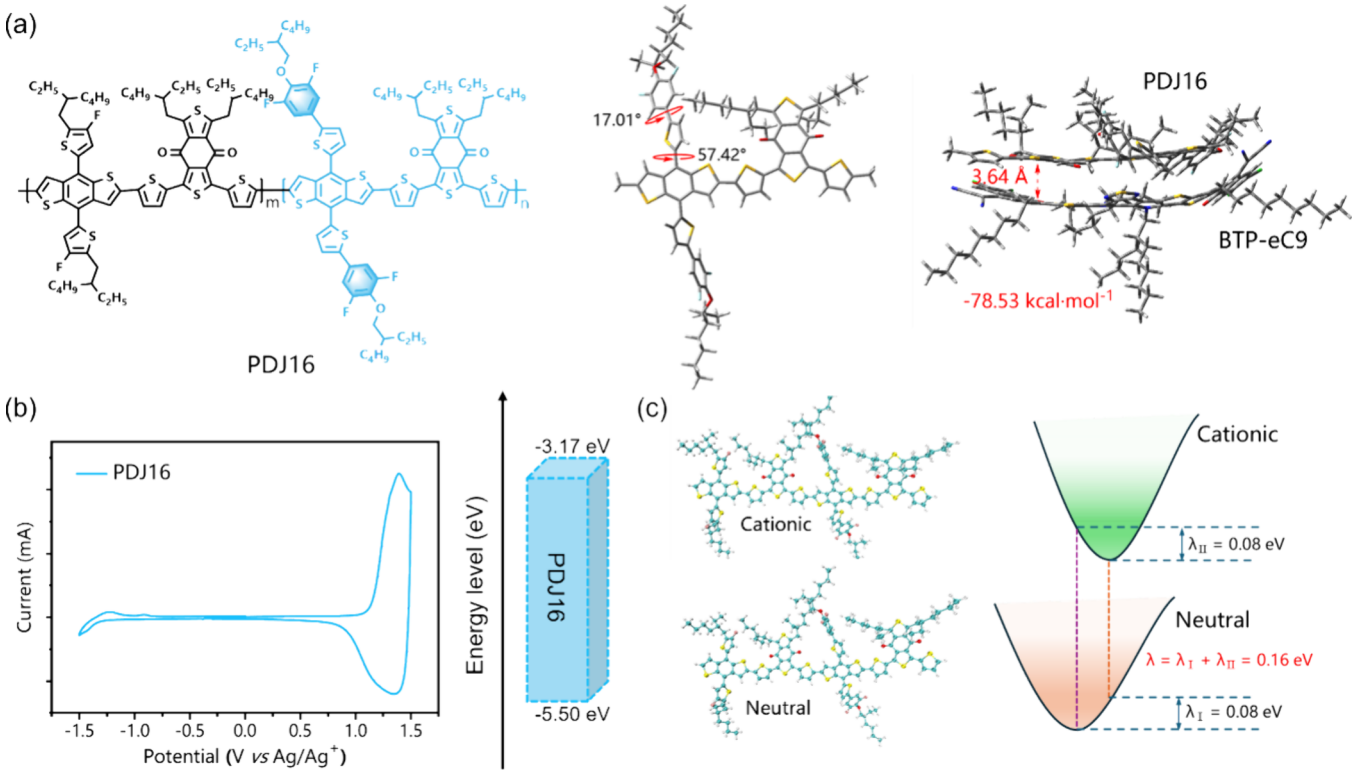

Figure 5. (a) Molecular structure of PDJ16, calculated dihedral angles between the conjugated backbone and the substituted phenyl side chains, and optimized intermolecular packing diagrams with BTP-eC9, (b) cyclic voltammetry data and corresponding energy levels, and (c) visualization of λ_h based on DFT-optimized cationic and neutral geometries.

https://doi.org/10.1021/acsaelm.6c01773
ACS Appl. Electron. Mater. 2026, 8, 9638−9646

Downloaded from pubs.acs.org/aaembp/article-pdf/8/21/9638/6907982/el-2026-01773w.pdf by CHALMERS UNIV OF TECHNOLOGY user on 23 November 2026

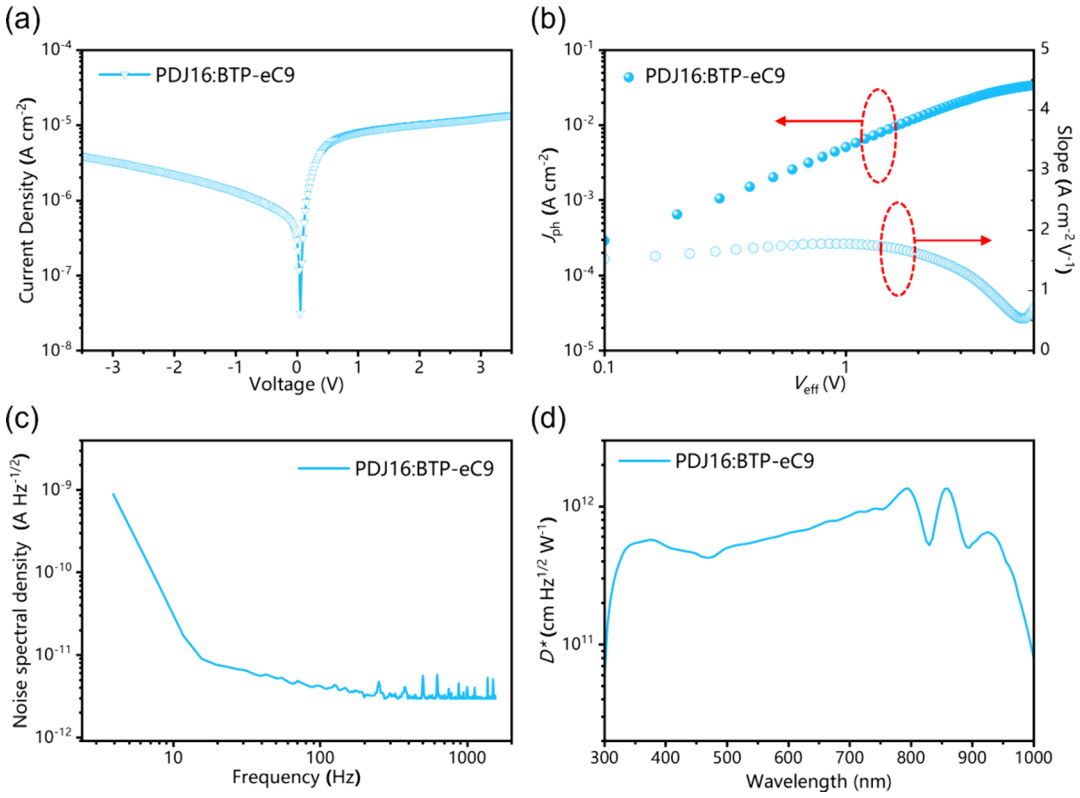

Figure 6. (a) Dark $J-V$ characteristics, (b) $J_{ph}-V_{eff}$ characteristics and corresponding slopes, (c) S_n at 1.0 V, and (d) $D^*(\lambda)$ at 1.0 V for the PDJ16:BTP-eC9 PM-OPD.

space-charge limited current (SCLC) measurements. For the hole-only device, the fitted $J^{1/2}-V$ characteristics yielded a μ_h of 2.1×10^{-4} cm^2 V^{-1} s^{-1} (Figure S7a). Similarly, for the electron-only device, a μ_e of 2.1×10^{-4} cm^2 V^{-1} s^{-1} was obtained (Figure S7b). Both mobility values for the PDJ16:BTP-eC9 blend layer were lower than those measured for the PM6:BTP-eC9 blend layer, following a similar trend observed in devices based on PDJ15:BTP-eC9 blend layer. The results suggest that the introduction of fluorinated sidechains via steric modulation in PDJ16 reduces carrier mobility, which in turn is expected to produce a lower dark current in the detector compared to PM6:BTP-eC9-based control device. The SCLC analysis of the PDJ16:BTP-eC9 PM-OPD confirms that donor-sidechain steric engineering in PDJ16 has similar impact on the device performance as seen with PDJ15, demonstrating the influence of this molecular engineering on the performance of the PM-OPDs.

In line with the molecular and charge transport analyses, the PDJ16:BTP-eC9 PM-OPD exhibited a lower dark current density of 8.0×10^{-6} A cm^{-2} (Figure 6a), resulting in a higher EQE of 2900% at 800 nm (Figure S8). The $J_{ph}-V_{eff}$ characteristics and slope analysis (Figure 6b) confirmed that the PDJ16:BTP-eC9 PM-OPD displays similar photomultiplication behavior observed in earlier measurements (Figure 3b). An S_n of 3.9×10^{-12} A Hz$^{-1/2}$ and a D^* of 1.4×10^{12} Jones at 800 nm were recorded (Figure 6c,d). Photoresponse time measurements further showed that the PDJ16:BTP-eC9 PM-OPD achieved τ_r and τ_f times of 1.7 and 7.3 ms, respectively (Figure S9), indicating structure-dependent carrier transport was preserved while maintaining rapid photoresponse compared to the PM6:BTP-eC9-based control device. These findings demonstrate that fluorinated steric modulation regulates carrier transport and trapping dynamics, thereby linking donor-side steric engineering to prolonged carrier trapping and enhanced photomultiplication in PM-OPDs.

3. CONCLUSIONS

In summary, donor-sidechain steric engineering was demonstrated as an effective strategy for enhancing NIR PM-OPD performance through dark current mitigation. Introducing monofluorinated alkoxylphenyl sidechains into the BDT-based PDJ15 donor increased conformational distortion, reduced packing density, and elevated hole reorganization energy, suppressing hole transport and prolonging trap retention. The resulting PDJ15:BTP-eC9 PM-OPD exhibited a high EQE of 5380%, responsivity of 34.5 A W^{-1} at 800 nm (1.0 V), a low dark current density of 1.4×10^{-6} A cm^{-2}, and detectivity of 4.6×10^{12} Jones, outperforming PM6-based controls. This fluorinated donor-side steric modulation advantage was further demonstrated with PDJ16, a structurally related analogue, via additional dark current reduction. Overall, donor-sidechain steric engineering represents a promising approach for designing high-gain, low-noise NIR PM-OPDs.

3.1. Experimental Section

Thiophene was lithiated with n-BuLi in anhydrous THF at −78 °C under argon, followed by reaction with benzo[1,2-b:4,5-b′]dithiophene-4,8-dione at 50 °C. Subsequent treatment with $SnCl_2 \cdot 2H_2O$ in 10% HCl afforded

https://doi.org/10.1021/acsaelm.6c01773
ACS Appl. Electron. Mater. 2026, 8, 9638−9646

Downloaded from pubs.acs.org/aaembp/article-pdf/8/21/9638/6907982/el-2026-01773w.pdf by CHALMERS UNIV OF TECHNOLOGY user on 23 November 2026

4,8-bis(thiophen-2-yl)benzo[1,2-b:4,5-b′]dithiophene. The terminal positions of the two thienyl groups were lithiated with n-BuLi at −78 °C and reacted with Me_3SnCl. The resulting distannylated intermediate was coupled with 1-bromo-3-fluoro-4-(2-ethylhexyloxy)benzene using $Pd(PPh_3)_4$ in anhydrous toluene at 100−110 °C. The obtained intermediate was subsequently lithiated at the 2,6-positions of the BDT core and treated with Me_3SnCl to afford the modified BDT-Sn monomer M2. Finally, the PM6-type BDT-S_n monomer M1 (0.080 mmol), M2 (0.020 mmol), and the dibrominated BDD monomer (0.100 mmol) were dissolved in anhydrous toluene (5 mL). After argon purging, $Pd(PPh_3)_4$ (5 mg) was added, and the mixture was stirred at 110 °C for 22 h. The crude polymer was precipitated in methanol, purified by silica-gel chromatography or Soxhlet extraction, reprecipitated in methanol, and dried under vacuum for 24 h to afford PDJ15.

PDJ16 was synthesized through an analogous synthetic route, in which M3, the difluorinated BDT-Sn monomer, was used in place of M2. The resulting polymer was purified and dried using the same procedure described above.

PM6 (poly[(2,6-(4,8-bis(5-(2-ethylhexyl-3-fluoro) thiophen-2-yl)-benzo [1,2-b:4,5-b′] dithiophene))-alt-(5,5-(1′,3′-di-2-thienyl-5′,7′-bis(2-ethylhexyl)benzo [1′,2′c:4′, 5′c′] dithiophene-4,8-dione)]), PDJ15 and PDJ16 were synthesized as random copolymer donors through Stille coupling polymerization. The copolymer composition was controlled by the feed ratio of the PM6-type BDT-Sn monomer and the bulky fluorinated phenyl-substituted BDT-Sn monomer. The corresponding m:n ratios were 8:2 for PDJ15 and PDJ16, respectively. BTP-eC9 (2,2′-((2Z,2′Z)-((12,13-bis(2-butyloctyl)-3,9-dinonyl-12,13-dihydro-[1,2,5]thiadiazolo [3,4-e]thieno[2″,3″:4′,5′] thieno [2′,3′:4,5]pyrrolo[3,2-g]thieno[2′,3′:4,5] thieno[3,2-b] indole-2,10-diyl)bis(methaneylylidene)) bis(5,6-dichloro-3-oxo-2,3-dihydro-1H-indene-2,1-diylidene))dimalononitrile).

OPDs were fabricated on indium tin oxide (ITO) glass substrates with a sheet resistance of 15 Ω per square. The ITO glass substrates were rinsed with standard procedure, subsequently were dried by utilizing pure nitrogen gas and treated by oxygen plasma lasted 15 min to improve its clearance and work function. Then, all the cleaned ITO glass substrates were transferred into a high-purity nitrogen-filled glove box. ZnO suspension was spin-coated on ITO substrates at 3000 rpm for 50 s Chloroform solution of PM6/PDJ15or PDJ16:BTP-eC9 mixture (7:100, w/w) was made as 30 mg/mL, the blends (donor:acceptor = 7:100) solution was drop-cast on the top of ZnO layer to prepare 300 nm thick active layers and then the wet active layers were directly dried at 120 °C for 30 min. Under 10^{-4} Pa in a vacuum chamber, 100 nm Ag film was finally deposited onto the active layers based on the thermal evaporation method. The active area of the OPDs is approximately 9 mm^2 in this study.

The monochromatic light source used in EQE measurement was generated by a Xenon lamp and the Bentham TMc300 monochromator. The forward bias used in the transient photoresponses measurements was controlled by the RIGOL DP821A power supply. Current vs voltage ($J-V$) characteristics of the PM-OPDs was recorded by using a Keithley-2400 source meter. The hole mobility (μ_h) and electron mobility (μ_e) of the neat PM6/PDJ15 or PDJ16 film and PM6/PDJ15or PDJ16:BTP-eC9 mixture (7:100, w/w) film, based single carrier devices were analyzed using the space charge−limited current technique. The charge transport mobility measurement reveals the mechanism for the reduction of dark current for PM OPDs. The LDR of the PM-OPDs was measured under monochromatic light of 680 nm generated by diode laser. The incident light intensity was manipulated by utilizing different neutral density filters.

■ ASSOCIATED CONTENT

Data Availability Statement

The supplementary material of this article contains the data that underpins the conclusions of this study.

Supporting Information

The Supporting Information is available free of charge at https://pubs.acs.org/doi/10.1021/acsaelm.6c01773.

Detailed synthetic procedure and synthetic route for PDJ15; synthetic route for PDJ16; NMR spectra; molecular-weight distribution; optical and electrochemical properties; computational methodology; charge-mobility measurements; and supplementary device-performance data (DOCX)

■ AUTHOR INFORMATION

Corresponding Authors

Donghong Yu − *Department of Chemistry and Bioscience, Aalborg University, Aalborg 9220, Denmark; Sino-Danish Center for Education and Research, Aarhus 8000, Denmark;* orcid.org/0000-0002-3035-5035; Email: yu@bio.aau.dk

Ergang Wang − *Department of Chemistry and Chemical Engineering, Chalmers University of Technology, Göteborg 41296, Sweden;* orcid.org/0000-0002-4942-3771; Email: ergang@chalmers.se

Furong Zhu − *Department of Physics, Research Centre of Excellence for Organic Electronics, Institute of Advanced Materials, Hong Kong Baptist University, Hong Kong 999077, Hong Kong, China;* orcid.org/0000-0002-6691-1937; Email: frzhu@hkbu.edu.hk

Authors

Jing Gao − *Department of Chemistry and Bioscience, Aalborg University, Aalborg 9220, Denmark;* orcid.org/0000-0001-6333-7258

Jingnan Wu − *Department of Chemistry and Chemical Engineering, Chalmers University of Technology, Göteborg 41296, Sweden*

Zhuangmiao Wang − *Department of Physics, Research Centre of Excellence for Organic Electronics, Institute of Advanced Materials, Hong Kong Baptist University, Hong Kong 999077, Hong Kong, China;* orcid.org/0009-0001-1498-6873

Yu Tang − *Department of Physics, Research Centre of Excellence for Organic Electronics, Institute of Advanced Materials, Hong Kong Baptist University, Hong Kong 999077, Hong Kong, China;* orcid.org/0000-0002-2719-3119

Complete contact information is available at: https://pubs.acs.org/doi/10.1021/acsaelm.6c01773

Notes

The authors declare no competing financial interest.

https://doi.org/10.1021/acsaelm.6c01773
ACS Appl. Electron. Mater. 2026, 8, 9638−9646

Downloaded from pubs.acs.org/aaembp/article-pdf/8/21/9638/6890798/2/el-2026-01773w.pdf by CHALMERS UNIV OF TECHNOLOGY user on 23 November 2026

■ ACKNOWLEDGMENTS

This work was financially supported by the Research Grants Council, General Research Fund (12304024, 12304225, and 12304326), the Guangdong Basic and Applied Basic Research Fund (2025A1515011509), Hong Kong Universities "1+1+1" Joint Research Collaboration Scheme (2025A0505000013). D.Y. acknowledges funding from the Sino-Danish Center (SDC) for Education and Research.

■ REFERENCES

(1) Liu, J.; Wang, Y.; Wen, H.; Bao, Q.; Shen, L.; Ding, L. Organic Photodetectors: Materials, Structures, and Challenges. *Sol. RRL* **2020**, *4*, 2000139.

(2) Lan, Z.; Lee, M.-H.; Zhu, F. Recent Advances in Solution-Processable Organic Photodetectors and Applications in Flexible Electronics. *Adv. Intell. Syst.* **2022**, *4*, 2100167.

(3) Zhao, Z.; Xu, C.; Niu, L.; Zhang, X.; Zhang, F. Recent Progress on Broadband Organic Photodetectors and Their Applications. *Laser Photonics Rev.* **2020**, *14*, 2000262.

(4) Ren, H.; Chen, J.-D.; Li, Y.-Q.; Tang, J.-X. Recent Progress in Organic Photodetectors and Their Applications. *Adv. Sci.* **2021**, *8*, 2002418.

(5) Wang, Q.; Zhang, Y.; Wei, Z. Recent Progress on Organic Near-Infrared Photodetectors: Mechanism, Devices, and Applications. *Chin. J. Chem.* **2023**, *41*, 958−978.

(6) Huang, J.; Fan, Q.; Jin, Z.; Zhang, H.; Dou, Z.; Wang, M.; Li, J.; Xu, L.; Zhou, G.; Zhang, T.; Chen, S. Optimizing Electron Injection Barriers and Hole-Trapping Ability for High-Performance Photomultiplication-Type Ternary Organic Photodetectors. *J. Appl. Phys.* **2024**, *135*, 063101.

(7) Suthar, G.; Hsiao, Y.-T.; Tsai, K.-W.; Liao, C.-Y.; Chu, C.-W.; Chang, Y.-M.; Chen, F.-C. Morphological Effects on the Performance of Broadband Organic Photomultiplication Photodetectors Containing Selenium-Substituted Non-Fullerene Acceptors. *Adv. Funct. Mater.* **2023**, *33*, 2301538.

(8) Yang, K.; Zhao, Z.; Liu, M.; Niu, L.; Zhao, X.; Yuan, G.; Ma, X.; Zhang, F. Highly Sensitive Broadband Photomultiplication-Type All-Polymer Photodetectors and Their Applications in Optical Pulse Counting. *J. Mater. Chem. C* **2022**, *10*, 10888−10894.

(9) Yang, K.; Wang, J.; Zhao, Z.; Sun, Y.; Liu, M.; Zhou, Z.; Zhang, X.; Zhang, F. Highly Sensitive Photomultiplication-Type Polymer Photodetectors by Manipulating Interfacial Trapped Electron Density. *Chem. Eng. J.* **2022**, *435*, 134973.

(10) Han, S. G.; Lee, H.; Choi, W.; Lee, D.; Kim, S.; Sung, Y.; Kim, S.; Cho, K. Photomultiplication-Type Organic Photodetectors with Fast Response Enabled by the Controlled Charge-Trapping Dynamics of a Quantum-Dot Interlayer. *Adv. Funct. Mater.* **2021**, *31*, 2102087.

(11) Liu, J.; Gao, M.; Kim, J.; Zhou, Z.; Chung, D. S.; Yin, H.; Ye, L. Challenges and Recent Advances in Photodiode-Based Organic Photodetectors. *Mater. Today* **2021**, *51*, 475−503.

(12) Zhao, Z.; Li, C.; Shen, L.; Zhang, X.; Zhang, F. Photomultiplication-Type Organic Photodetectors Based on Electron Tunneling Injection. *Nanoscale* **2020**, *12*, 1091−1099.

(13) Huang, J.; Lee, J.; Schrock, M.; Dixon, A. L.; Lill, A. T.; Cho, K.; Bazan, G. C.; Nguyen, T.-Q. Large-Gain, Low-Voltage, and Wideband Organic Photodetectors via Unbalanced Charge Transport. *Mater. Horiz.* **2020**, *7*, 3234−3241.

(14) Shan, C.; Wang, Y.; Luo, D.; Dai, T.; Xu, X.; Gu, X.; Xu, X.; Zhou, E.; Zhao, T.; Kyaw, A. K. K. High Detectivity in Photomultiplication-Type Organic Photodetectors: A Study on EQE and Dark-Current Balance via Processing Methods. *Adv. Mater. Technol.* **2025**, *10*, 2401574.

(15) Sarwar, A.; Wang, Y.; Winkler, L. C.; Zhang, T.; Schröder, J.; Spoltore, D.; Leo, K.; Benduhn, J. Tailoring Hole-Blocking Layers Enables a Versatile Approach for Fast Photomultiplication-Type Organic Photodetectors. *Adv. Funct. Mater.* **2025**, *35*, 2424456.

(16) Yang, W.; Qiu, W.; Georgitzikis, E.; Simoen, E.; Serron, J.; Lee, J.; Lieberman, I.; Cheyns, D.; Malinowski, P.; Genoe, J.; Chen, H.; Heremans, P. Mitigating Dark Current for High-Performance Near-Infrared Organic Photodiodes via Charge Blocking and Defect Passivation. *ACS Appl. Mater. Interfaces* **2021**, *13*, 16766−16774.

(17) Wang, J.; Deng, S.; Ma, J.; Hu, J.; Liu, J. n-Type Polythiophene as a Hole-Blocking Layer in Inverted Organic Photodetectors. *Giant* **2024**, *19*, 100291.

(18) Hu, X.; Qiao, Z.; Nodari, D.; He, Q.; Asatryan, J.; Rimmele, M.; Chen, Z.; Martín, J.; Gasparini, N.; Heeney, M. Remarkable Isomer Effect on the Performance of Fully Non-Fused Non-Fullerene Acceptors in Near-Infrared Organic Photodetectors. *Adv. Opt. Mater.* **2024**, *12*, 2302210.

(19) Lin, H.; Xu, B.; Wang, J.; Yu, X.; Du, X.; Zheng, C.-J.; Tao, S. Novel Dark-Current Reduction Strategy via Deep Bulk Traps for High-Performance Solution-Processed Organic Photodetectors. *ACS Appl. Mater. Interfaces* **2022**, *14*, 34891−34900.

(20) Deng, B.; Lu, K.; Lu, Z.; Li, Y.; Dai, G.; Yin, L.; Wang, Z.; Grandidier, B.; Xu, T.; Zhu, F. Visible-Blind Near-Infrared Organic Vision Sensors for Imaging in Adverse Environmental Conditions. *Adv. Opt. Mater.* **2026**, e71858.

(21) Tang, Y.; Wang, Z.; Gao, M.; Han, J.; Yuan, L.; Zhu, F. Dual-Mode Narrowband Organic Photodetectors for Self-Aligned Imaging in NIR-I and NIR-II. *Nat. Commun.* **2025**, *16*, 7144.

(22) Lan, Z.; Lei, Y.; Chan, W. K. E.; Chen, S.; Luo, D.; Zhu, F. Near-Infrared and Visible-Light Dual-Mode Organic Photodetectors. *Sci. Adv.* **2020**, *6*, eaaw8065.

(23) Wang, W.; Zhang, F.; Bai, H.; Li, L.; Gao, M.; Zhang, M.; Zhan, X. Photomultiplication Photodetectors with P3HT:Fullerene-Free Material as the Active Layers Exhibiting a Broad Response. *Nanoscale* **2016**, *8*, 5578−5586.

(24) Ma, Y.; Xu, X.; Li, T.; Wang, Z.; Li, N.; Zhao, X.; Wei, W.; Zhan, X.; Shen, L. Amplified Narrowband Perovskite Photodetectors Enabled by Independent Multiplication Layers for Anti-Interference Light Detection. *Sci. Adv.* **2025**, *11*, eadq1127.

(25) Miao, J.; Zhang, F.; Lin, Y.; Wang, W.; Gao, M.; Li, L.; Zhang, J.; Zhan, X. Highly Sensitive Organic Photodetectors with Tunable Spectral Response under Bi-Directional Bias. *Adv. Opt. Mater.* **2016**, *4*, 1711−1717.

(26) Guo, D.; Yang, D.; Zhao, J.; Agafonov, V.; Ma, D. Role of Interfaces in Controlling Charge Accumulation and Injection in the Photodetection Performance of Photomultiplication-Type Organic Photodetectors. *J. Mater. Chem. C* **2020**, *8*, 9024−9031.

(27) Liu, M.; Yao, Q.; Li, S.; Qin, Y.; Jeong, S. Y.; Ma, Y.; Shen, L.; Ma, X.; Yang, K.; Yuan, G.; Woo, H. Y.; Zhang, F. Interfacial Engineering for Photomultiplication-Type Organic Photodetectors with Signal-to-Noise Ratio over 89,000. *Adv. Opt. Mater.* **2024**, *12*, 2303216.

(28) Lan, Z.; Lau, Y. S.; Wang, Y.; Xiao, Z.; Ding, L.; Luo, D.; Zhu, F. Filter-Free Band-Selective Organic Photodetectors. *Adv. Opt. Mater.* **2020**, *8*, 2001388.

(29) Wang, Z.; Tang, Y.; Han, J.; Zhu, F. Visible-Blind Near-Infrared Organic Photodetectors. *Appl. Phys. Lett.* **2024**, *124*, 021103.

(30) Lu, K.; Deng, B.; Lu, Z.; Jiang, Y.; Wang, Z.; Wang, X.; Xu, T.; Zhu, F. High-Performance Inverted Near-infrared Organic Photodetectors Enabled by Interface Passivation and Optical Engineering. *ACS Appl. Electron. Mater.* **2026**, *8*, 6831−6839.

(31) Li, N.; Lan, Z.; Lau, Y. S.; Xie, J.; Zhao, D.; Zhu, F. SWIR Photodetection and Visualization Realized by Incorporating an Organic SWIR-Sensitive Bulk Heterojunction. *Adv. Sci.* **2020**, *7*, 2000444.

(32) Li, Y.; Han, J.; Zaman, N.; Wang, T.; Tang, Y.; Cheung, S. H.; Wang, Z.; Sarkar, R.; Vasenko, A. S.; Prezhdo, O. V.; Gutsev, G. L.; Zhang, K.; Gutsev, L. G.; Xu, X.; Zhu, F. Thermodynamic Stabilization of PbS Quantum Dots for High-Performance Short-Wave Infrared Photodetection. *ACS Appl. Mater. Interfaces* **2026**, *18*, 54241−54251.

(33) Gao, J.; Wang, Z.; Tang, Y.; Han, J.; Gao, M.; Wu, J.; Chen, Q.; Yu, D.; Wang, E.; Zhu, F. Mitigating Dark Current in Photomultiplication Organic Photodetectors via the Charge-Trap-Gradient Bulk Heterojunction. *ACS Appl. Mater. Interfaces* **2025**, *17*, 52426−52434.

Downloaded from pubs.acs.org/aaembp/article-pdf/8/21/9638/6890798/2/el-2026-01773w.pdf by CHALMERS UNIV OF TECHNOLOGY user on 23 November 2026

https://doi.org/10.1021/acsaelm.6c01773
ACS Appl. Electron. Mater. 2026, 8, 9638−9646